Surface atomic layer fluorination of Li4Ti5O12: Investigation of the surface electrode reactivity and the outgassing behavior in LiBs

Youn Charles-Blin, Olinda Gimello, Delphine Flahaut, Katia Guérin, Marc Dubois, Laure Monconduit, Nicolas Louvain, Hervé Martinez

To cite this version:

Youn Charles-Blin, Olinda Gimello, Delphine Flahaut, Katia Guérin, Marc Dubois, et al.. Surface atomic layer fluorination of Li4Ti5O12: Investigation of the surface electrode reactivity and the outgassing behavior in LiBs. Applied Surface Science, 2020, 527, pp.146834. 10.1016/j.apsusc.2020.146834 . hal-02881897

HAL Id: hal-02881897
https://hal.science/hal-02881897

Submitted on 10 Nov 2023

Surface Atomic Layer Fluorination of $Li_4Ti_5O_{12}$: investigation of the surface electrode reactivity and the outgassing behavior in LiBs.

Youn Charles-Blin,[♠♡¥] Delphine Flahaut,[♡¥*] Katia Guérin,[‡] Marc Dubois,[‡] Laure Monconduit,[♠¥] Nicolas Louvain,[♠¥*] Hervé Martinez[♡¥]

[♠]Institut Charles Gerhardt Montpellier, Université de Montpellier, CNRS, Montpellier (France).

[♡]Univ, Pau & Pays Adour / E2S UPPA, Institut des Sciences Analytiques et de Physicochimie pour l'Environnement et les Matériaux – UMR 5254, 64000 Pau, France

[‡]Université Clermont Auvergne, CNRS, Sigma Clermont, ICCF, 63000 Clermont-Ferrand, France.

[¥]Réseau sur le Stockage Electrochimique de l'Energie (RS2E), FR CNRS 3459, 33 Rue Saint Leu, 80039 Amiens, France.

Corresponding authors

Delphine Flahaut

*E-mail: delphine.flahaut@univ-pau.fr.

Univ, Pau & Pays Adour / E2S UPPA, Institut des Sciences Analytiques et de Physicochimie pour l'Environnement et les Matériaux – UMR 5254, 64000 Pau, France

+33 540175006

Nicolas Louvain

*E-mail: nicolas.louvain@umontpellier.fr.

Institut Charles Gerhardt Montpellier, Université de Montpellier, CNRS, Montpellier (France).

+33 467143309

Abstract

This paper presents the interest of the surface fluorination of $Li_4Ti_5O_{12}$ anode material in Li-ion batteries by decomposition of solid XeF_2. Enhanced electrochemical behaviors are observed for the most fluorinated material: both specific capacities (by 12 % for 100 cycles) and C-rate capability are improved. The $Li_4Ti_5O_{12}$/electrolyte interface interactions conduct usually to side reactions and gas generation. *Operando* ATR-FTIR and GC-MS analysis carried out show that the fluorination fades the catalytic properties of Ti^{4+} and thus reduces the CO_2 gas generation by 5 times during the first cycle. Indeed, the fluorination of $Li_4Ti_5O_{12}$ protects the surface from the formation of a solid electrolyte interface by the formation of Li-F passivating layer. XPS analysis demonstrate that the passivation is effective to protect the surface of the electrodes from carbonates and salt degradation products during the first cycles, which are determinant for batteries life span.

Keywords

$Li_4Ti_5O_{12}$; Fluorination; Li-ion battery outgassing; SEI; XPS; *Operando* ATR-FTIR.

Highlights

- Atomic layer fluorination of $Li_4Ti_5O_{12}$ particles by the mean of XeF_2
- Galvanostatic and C-rate improvements after fluorination
- Operando monitoring of the electrolyte by ATR-FTIR
- Surface fluorination is effective to reduce the CO_2 gas generation by 5 times
- Surface fluorination reduces the formation of LiF and carbonates in the SEI

1. Introduction

In Li-ion batteries, Li^+ ions and electrons are shuttling between negatives and positive host structure separated by the electrolyte. Usually, negative materials are working at low potentials close to 0 V *vs.* Li^+/Li whereas positive materials work at high potentials, above 3 V *vs.* Li^+/Li. Such low operating voltage for negative electrodes turned up to be problematic since electrolytes are thermodynamically unstable against reduction. The electrolyte instability leads to side reactions and subsequently to the formation of a Solid Electrolyte Interphase (SEI) at the negative electrode surface. The SEI creation consumes Li^+ ions and increases the impedance of the battery, but in the same time the formation of a stable SEI, conductive to Li^+ and electronically insulating is critical to ensure high coulombic efficiency, good life span and safety.

Hence, the research focused on the development of lithiated titanate material working at relatively high potential to avoid electrolyte reduction issues. In the late 80s, Colbow *et al.*[1] discovered the electrochemical properties of lithiated titanate phase and later on Ohzuku *et al.*[2] evidenced the "zero strain" behavior of the $Li_4Ti_5O_{12}$ (LTO) phase. Since then and despite a rather low specific capacity (175 $mAh.g^{-1}$), LTO anode material was considered as a potential alternative to carbon graphite, thanks to its very high rate capability, phenomenal life span and good safety.[3] But above all, it was commonly admitted that thanks to the relatively high working potential of the LTO (1.55 V *vs.* Li^+/Li) SEI could not be formed on electrodes surfaces.[4,5] However, recent studies have proved that SEI is formed on LTO based anode,[6] putting down the belief that a working potential above 1.0 V *vs.* Li^+/Li is enough to prevent the electrolyte reduction.[7] Furthermore, the starting $Li_4Ti_5O_{12}$ compound exhibits poor electronic conductivity (approximately 10^{-13} S cm^{-1})[8] and moderate lithium diffusion coefficient (approximately 10^{-9} to 10^{-13} cm^2 s^{-1}),[9] slowing down electrochemical reactions during the first cycle. As well, the surface of LTO appears to react with the electrolyte via well-known catalytic Ti^{4+} ions, producing rather strong outgassing.[10] All these roadblocks exclude the LTO from wide broadcasted anode material market.

Efforts have been deployed to develop sustainable strategies to overcome low conductivity, SEI formation and outgassing issues. Since the LTO working potential is high, most of the reductive additives such as fluoroethylene carbonate (FEC) reveal to be ineffective, [11] conducting to other strategies. Downsizing to nanoparticles provides enhanced electronic percolation but in the other hand the specific area is drastically increased leading to exalted surface reactivity.[12,13] Carbon coatings are developed to both improve the electronic conductivity and prevent gas generation mostly because gassing is neglectable for graphite electrodes.[10,14] Coated LTO improves rate capability at room temperature and at 55°C.[15,16] But the nature of carbon coating drives to similar surface reactivity to graphite electrode and thus to SEI formation. Other coating materials than carbon have been investigated to solve the gassing problem among which zinc oxide ZnO,[17] AlF_3,[18] NiO_x,[19] and TiN_x.[20] Ionic conductor Li_3PO_4 coatings show both slightly improved C-rate capability and reduced CO_2 outgassing but several synthesis steps are required to obtain a dense thin film.[21] Several others coating materials have been assessed in the literature, among which the fluorine. Nakajima *et al.*[22] were the first to consider, in the late 90s, the fluorine as a potential electrode protection against SEI formation on graphite material. Later on, studies have been conducted on the fluorination of LTO by the mean of F_2 gas or by solid state reaction with NH_4F.[23,24] In both cases, slight increase of the specific capacity and improvement of the rate capability are noted. In the case of the fluorination by NH_4F, the authors correlate the improved electrochemical behavior to better conduction properties that come from the formation of a mixed valence Ti^{4+}/Ti^{3+}. However, the interface reactivity with the electrolyte and the SEI formation on fluorinated electrodes were not addressed by these studies, neither the gas generation, yet known as a current issue for LTO. The surface fluorination of LTO should influence the Ti^{4+} catalytic properties and thus the gas formation within the cells.

In this study, we report surface fluorinations of LTO using a one-shot synthesis performed at room temperature using XeF_2 as fluorine source. This process allows a simpler and reproducible route to fluorinate the electrode materials without complex operations usually necessary for gaz process. The modifications on the LTO material induced by the fluorination are widely described and discussed in a previous study[25]. We demonstrated by XPS and

HMQC that the fluorination of LTO leads to mainly form Li-F environments on particles surface, in which Li^+ ions are surrounded by 3 fluorine atoms. Moreover, the increasing formation of a $Li_{4-x}Ti_5O_{12-x}F_x$ solid solution, chemically close to the $TiOF_2$ compound, is observed with higher content of fluorine. We also evidenced by AES that the fluorinated layer is between 100 and 200 nm thick. Electrochemical improvements are noted upon galvanostatic cycling and for rate capability for fluorinated electrodes. The impact of the fluorination on the lithium solvation shells is assessed by *operando* ATR-FTIR measurements within the electrolyte in the near electrode surface. In addition, we investigate by ATR-FTIR and GC-MS, the CO_2 gas generation within the electrolyte and the fluorination impact on this gas production upon cycling. Moreover, the influence of the fluorination on the surface electrode reactivity and the resulting SEI composition are studied upon cycling by the mean of XPS analysis using two different depth probe (Al and Ag X-Ray sources).

2. Material and methods

Chemicals. Lithium titanate ($Li_4Ti_5O_{12}$) nanopowder, < 200 nm particle size, 99.7 % trace metal basis), xenon difluoride (XeF_2, 99.99 % trace metal basis), and lithium metal ribbon (Li, 99.9 % trace metal basis) were purchased from Sigma-Aldrich. The carbon black Super P C65 additive was purchased from Imerys. $LiPF_6$ 1 M in EC:DMC (1:1 vol.%) electrolyte (99.9 %, H_2O < 20 ppm) was purchased from Solvionic. GE Healthcare Life Sciences Whatman Grade GF/D glass microfiber filters (borosilicate; ∅ 55 mm, 675 µm thickness) were purchased from Sigma-Aldrich.

Fluorination. All the synthesis were performed in polytetrafluoroethylene (PTFE) crucible sealed in an Argon filled glove box (O_2 and H_2O rate below 0.5 ppm) at room temperature. The PTFE is assumed to be inert toward the fluorinating agent. The LTO powder was exposed to the xenon difluoride for 1.5 hrs or 3.5 hrs corresponding to *LowF* and *HighF* samples respectively. These two fluorination conditions are selected since they conduct to contrasted results. Others fluorination conditions were tested, however higher fluorination content does not necessarily provide better electrochemical performances. The containers were opened in the glove box to stop the reaction. The LTO powder samples were fluorinated thanks to the controlled decomposition of solid XeF_2 and the following equilibrium:

$$XeF_2\,(s) = XeF_2(g) \qquad (1)$$

The Xenon difluoride is easily decomposed at the surface of a reactive material, releasing $F^{\bullet}$ at a constant and moderate rate because of the low saturating vapor pressure (measure up to 3.8 mmHg at 25°C and 318 mmHg at 100°C).[26]

$XeF_2\ (g) = Xe(g) + 2\ F^{\bullet}$ (2)
$2\ F^{\bullet} = F_2\ (g)$ (3)

Electrochemical characterizations. The electrochemical behavior of fluorinated materials is assessed in half-cell using lithium metal in coin cell 316L stainless steel CR2032 type. Before cycling characterization, 2 hrs of OCV were performed to stabilize the potential of the cells above 2.8 V. The charge and discharge specific capacities were measured at C-rate 1C (current density of 60 $mA.g^{-1}$) and the potential window was limited between 1.0 V and 2.5 V *vs.* Li^+/Li. The C- rate capability was observed for C rates 0.2C, 0.5C, 1C, 2C, 5C, 10C and 15C, with 5 full cycles performed at each rate to stabilize the capacities. The electrodes were prepared with 90 wt% of active material LTO, 5 wt% of carbon black and 5 wt% of Polyvinylidene difluoride (PVDF) used as mechanical binder. To evaluate the fluorination influence, all the fluorinated electrodes have been systematically compared with bare commercial LTO based electrode, using exactly the same galvanostatic conditions. All the tests were performed at room temperature regulated at 25°C. Subsequently, the coin cells were opened in glovebox and the electrodes were collected to be washed in pure DMC to remove exceeding salt and electrolyte on the surface. This step was mandatory to access to the SEI layer by the mean of the XPS, we consider that the SEI is not altered by this rinsing step.

Extreme Surface characterization. X-ray photoelectron spectroscopy (XPS) analyses were carried out by the mean of an ESCALAB 250 Xi spectrometer with a monochromatic Al-Kα X-ray source (hυ = 1486.6 eV) probing between 5 to 10 nm of the surface (~95% of the signal is originating from the first 5 nm) and a monochromatic Ag-Lα (hυ = 2984.3 eV) probing up to 18 nm in depth. The analysis of a 400×400 mm^2 area of the sample was done employing 20 eV as pass energy and 0.1 eV as energy step for the core peaks. Electron flood gun was used for charge compensation. The quantifications were done using CASA XPS software, after Shirley-type[27] background subtraction, by utilizing the Thermo Fisher Scientific Advantage cross-section database. The apparatus is directly connected to a glovebox, allowing us to transfer the powders under argon inert atmosphere with oxygen and moisture under 0.5 ppm.

Electrolyte characterization. The *operando* Attenuated Total Reflection Fourier-Transform Infrared spectroscopy (ATR-FTIR) analyses were performed in a home-made ATR experimental setup allowing both IR and electrochemical measurements in the same time. The electrodes were drilled in the middle using a sharp punch of ¼ inch, and placed over the ATR crystal. In this way, direct contact with the ATR crystal and the electrolyte was possible, the electrolyte analyzed area was considered to be in the neighborhood of the electrode. The electrodes were cycled in regard to lithium metal and with a whatman separator is the same cycling conditions than coin cells. The drilled electrodes were electrochemically tested in this cell and no modification of the behavior or specific capacities is observed. The spectra were recorded from 650 cm^{-1} to 4000 cm^{-1}, a wave number window in which the ATR crystal is transparent, with a 1 cm^{-1} resolution. An automatic program performs spectra recording, each spectrum acquisition was 30 seconds long, a time scale much shorter than the phenomena occurring in the cycling electrochemical cell. The starting time of the IR analysis was synchronized with the galvanostatic cycling.

Electrolytes were collected from cycled “swagelock” cells stopped at different state of charge (SOC), fully charged or discharged after the first cycle and diluted in 3 mL of high purity acetonitrile to be analyzed by Gas chromatography-mass spectrometry (GC-MS). GC-MS analyses were performed with a Shimadzu GCMS QP-2010 Plus apparatus. A Supel-Q-Plot colon silicon based with a divinylbenzene phase was used because it effectively resolves C1-C4 hydrocarbons species, among which outgassing that we expect to observe. The colon was heated up to 250°C with a 10°C/min ramp, the species were injected with a split ratio equal to 60. The MS stage was switched off between 10 and 13.5 min during the elution of very intense acetonitrile peak.

3. Results and discussions

3.1. Electrochemical behavior of fluorinated LTO

To assess the fluorination impact on the electrochemical behavior of LTO, a comparison of charge/discharge capacities at 1C rate for one hundred cycles and at different C-rates (0.2C, 0.5C, 1C, 2C, 5C, 10C and 15C) is shown figure 1 a and b.

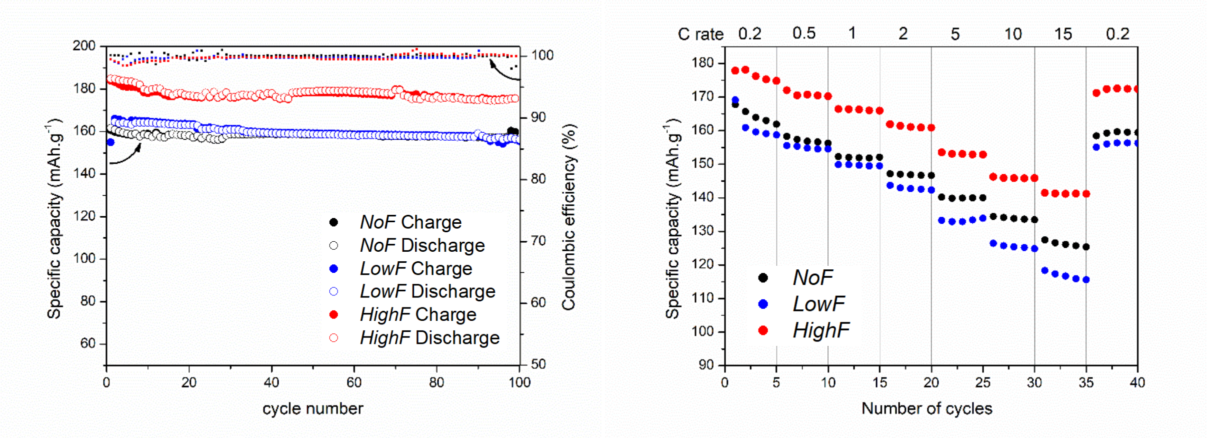

Figure 1 : a) charge (full bullet) and discharge (empty bullet) specific capacities of fluorinated and bare LTO samples at C-rate 1C for 100 cycles; b) specific capacity of fluorinated LTO and bare LTO samples at different current densities.

The specific capacities of bare LTO electrodes are observed at 160 ± 16 $mAh.g^{-1}$with a very good cyclability for the first 100 cycles (figure 1 a). This specific capacity of bare compound are lower than the theoretical specific capacity which can be expected with non-carbon-coated and non-annealed LTO material. The *LowF* LTO based electrodes exhibit a slightly higher specific capacities, around 165 ± 16.5 $mAh.g^{-1}$ for the first 30 cycles but then the capacities are actually very similar to the bare compound. In the case of the *HighF* LTO, specific capacities around 180 ±18 $mAh.g^{-1}$ are observed, which is 12% higher than the bare LTO. Notice that few instabilities are observed with *HighF* electrodes but overall the specific capacities remain higher. The extra capacity may coming from reduced surface reactivity of fluorination LTO as well as from the fluorinated solid solution $Li_{4-x}Ti_5O_{12-x}F_x$ that we previously identified in a previous study[25] and on Ti 2p spectra (figure S4), bringing new electrochemical properties . The coulombic efficiencies of the first cycle are affected by the fluorination as bare LTO electrodes provides 99.97 % against 99.49 % for the *HighF* compound. The fluorination provides a slightly lower coulombic efficiency for the few first cycles when a 1 C C-rate is applied straight away. In the case of a slower first cycle at 0.2 C C-rate, we observed the opposite trend with fluorinated electrode providing specific capacities close to the theoretical limit. From these observations, it appears clearly that a first cycle performed at low C-rate is required to settle down the LTO fluorinated surface lithium insertion channels.

C-rate measurements were performed to assess the rate capability for all the compounds. The *NoF* LTO exhibit already very good rate capability, with a remaining specific capacity of 125 ± 12.5 $mAh.g^{-1}$ at 15 C (figure 1 b). Indeed, LTO material is known for its very high rate cycling properties. But in this case these properties are enhanced by the fact that electrodes have relatively low loadings (1.5 mg.cm²) providing thin and very well percolated electrodes in which LTO is highly accessible. In thus configuration, the lithium diffusion coefficient within the electrode is not limiting the lithium insertion. Nevertheless, fluorinated compounds exhibit contrasted behavior in rate capability. *LowF* electrodes provide similar specific capacities to the *NoF* ones until 1 C rate. For higher rates, the *LowF* compound undergoes stronger capacity fading, to show un-stabilized specific capacity around 115 ± 11.5 mAh.g^{-1}. The lower specific capacities of *LowF* electrodes could be related to their systematically higher polarization voltage (table 1). The high *LowF* polarization strongly impact the galvanostatic curves as observed in figure 2. In contrary, the *HighF* electrodes exhibit the best rate capability, from the low C-rates to the highest ones. At 15 C, specific capacities of the *HighF* compound are measured up to 141 ± 14.1 mAh.g^{-1}, 13 % higher than the *NoF* ones. Also, the specific capacities remain very stable for the five cycles at this rate. After the rate capability measurements, all the compounds nearly regain their starting performances. From these electrochemical measurements, LTO *HighF* electrodes provides the best electrochemical performances.

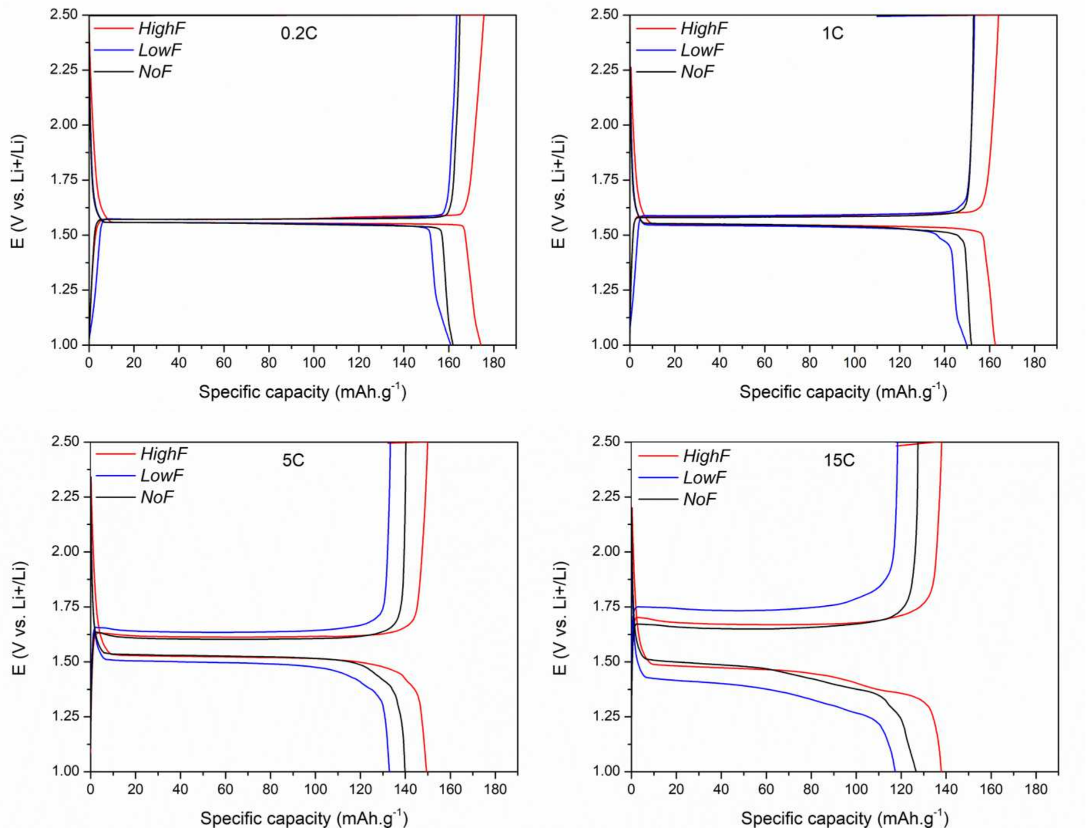

Figure 2 : Galvanostatic curves recorded at 0.2 C, 1 C, 5C and 15 C between 1 V and 2.5 V vs Li$^+$/Li for NoF (in black), LowF (blue) and HighF (red) electrodes.

Table 1 : Polarization voltage (V) of the NoF, LowF and HighF electrodes at different C-rates.

	Polarization (V) measured at ½Q Uncertainty ≈5 µV		
C-rate	*NoF*	*LowF*	*HighF*
0.2 C	0.021	0.019	0.018
0.5 C	0.020	0.021	0.018
1 C	0.038	0.052	0.041
2 C	0.049	0.076	0.056
5 C	0.080	0.146	0.093
10 C	0.140	0.266	0.157
15 C	0.233	0.414	0.222

1.1. Fluorination influence on the electrolyte and outgassing

To perform such characterizations, our choice focused on GC-MS coupled with ATR-FTIR measurements since these techniques provide great complementarities in gas generation and battery decay upon cycling investigation[28].

Operando ATR-FTIR electrolyte and gassing monitoring

To investigate the electrolyte evolution during cycling, ATR-FTIR measurements are carried out into the electrolyte in *operando* conditions, in the immediate neighborhood of the electrode. In addition, the ATR-FTIR is able to monitor the gas generation into the electrolyte. In order to identify the species present in the electrolyte (EC:DMC 1M $LiPF_6$), the spectra of the pure EC, DMC and electrolyte are recorded in the same conditions (figure S1). All the IR bands are attributed to vibrational transitions belonging to the species according to the literature[29–34]. We determine two main IR windows of interest, the first one between 1440 and 1100 cm^{-1} gives a good insight of lithium solvation into the electrolyte while the second one (950 and 650 cm^{-1}) is representative of the CO_2 outgassing production. The IR results are displayed figure 3 and 4 in relative intensity, in order to highlight the concentration evolution within electrolyte at the end of a charge or a discharge of the cell. If a $\frac{\Delta R}{R}$ appears positive, the related species concentration is increasing and *vice versa*.

In the first energetic window (1400-1100 cm^{-1}) displayed figure 3, both EC and DMC vibrational bands are observed: at 1390 cm^{-1} corresponding to bending $\delta(CH_2)$ in EC, at 1260 cm^{-1} corresponding to stretching ν(O-C-O) in DMC and at 1153 cm^{-1} attributed to stretching *v*(C-O) in EC. For each band, an additional blue-shifted band is observed, originated from the Li^+ solvation. Indeed, Li^+ are known to have coordination interactions with the most electronegative oxygen of the EC or DMC, strong interactions created leading to modify the force constant of intramolecular bonding[35–37]. Moreover, both pure DMC bands and DMC—Li^+ have higher intensities than the EC bands. Theoretical studies, carried out in the the second order Møller-Plesset perturbation theory (MP2/6-311+G(2d,p)), calculated the solvation energy of Li^+ of pure DMC equal to - 40.8 kcal.mol^{-1} while the solvation energy of pure EC is equal to -47.1 kcal.mol^{-1} [38,39]. Thus, the solvation with EC is favored and DMC—Li^+ solvation shells are weaker in comparison, explaining the stronger intensities of solvation/desolvation for DMC in charge/discharge. During the 1st discharge, the electrolyte of the *NoF* electrode exhibits DMC—Li^+ and EC—Li^+ desolvation while in charge the opposite process is not totally completed. It proves that a part of the solvation/desolvation process is not fully reversible in disfavor of the solvation. The fact that less and less solvation shells is formed could be related to irreversible lithium losses. The second cycle exhibits even less reversibility in solvation/desolvation process, the pure DMC and EC related bands remain barely positives in discharge. After tenth cycles in regard of the LTO *NoF* electrode, the electrolyte shows no longer reversible processes since the charge and discharge spectra are superimposed and show no more antagonist DMC or EC solvation/desolvation bands. The IR spectra of electrolytes cycled in regard of *HighF* electrodes exhibit stronger solvation/desolvation and much better reversibility throughout the tenth first cycles. Indeed, the solvation/desolvation bands of both DMC and EC remain antagonist with opposite signs in charge/discharge. It seems that the fluorination has no impact on the coordination shell intramolecular energy since no significant shifts are observed. We consider that the fluorination affects the intermolecular energy of the solvation shells and contributes to the stronger solvation/desolvation processes in the neighborhood of the electrode. The modified solvation intermolecular interactions may also lead to impact the reduction potential of solvents and thus the SEI formation.

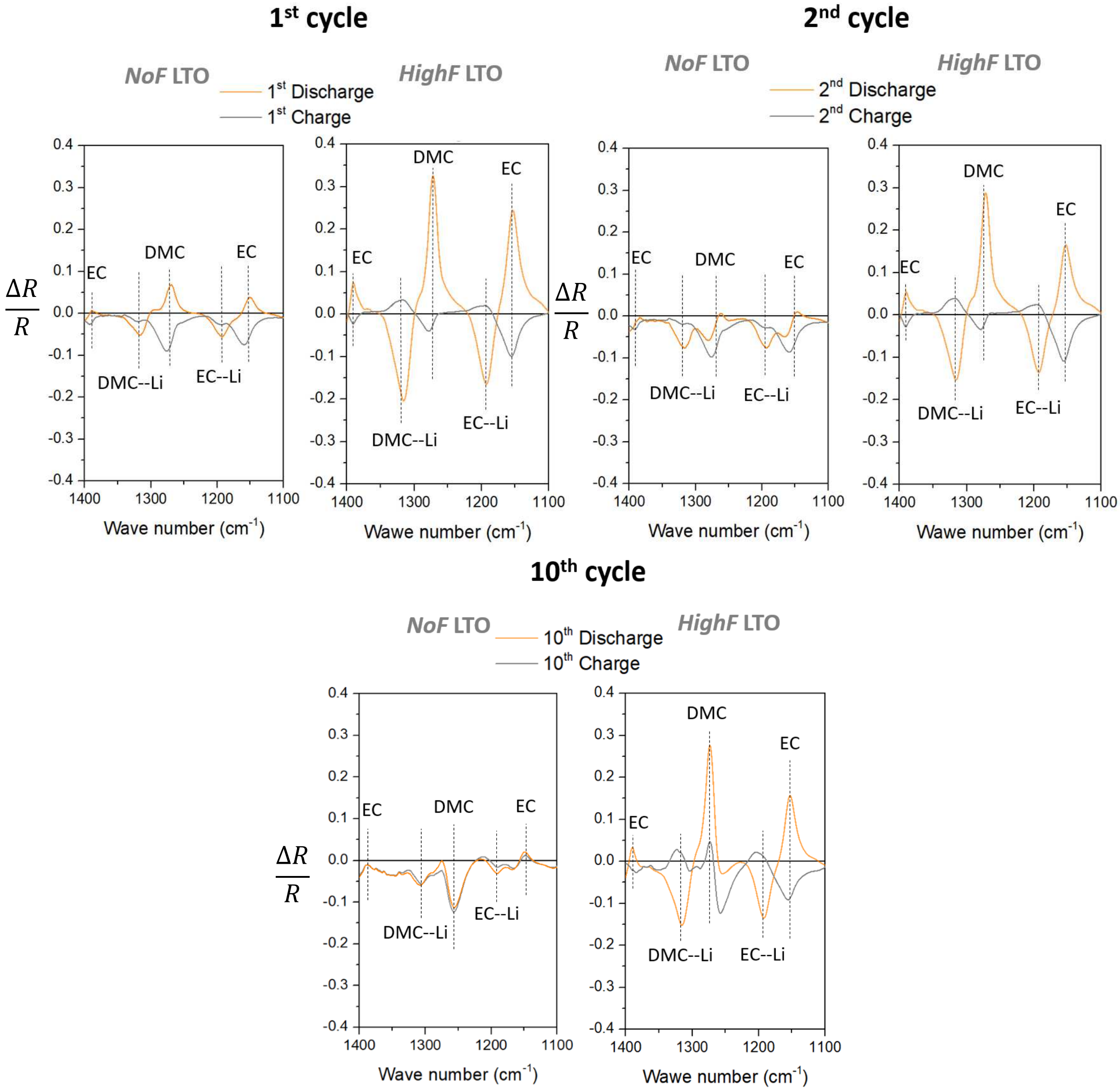

Figure 3 : ATR-FTIR spectra recorded between 1400 and 1100 cm^{-1} for electrolytes LP30 without additives in the neighborhood of NoF and HighF electrodes for the 1st, 2nd and 10th charge (in grey)/discharge (in orange) cycle. The spectra are displayed in relative intensities: positive bands for formed species and negative bands for consumed species.

In the second energetic window of interest (950 – 650 cm^{-1}), a stretching *ν*(P-F) band originated from $LiPF_6$ salt is observed at 839 cm^{-1}. This band is partially overlapped by blue-shifted bending *δ*(OCO_2) band belonging to the DMC. One additional bending *δ*(OCO_2) band from EC is also observed at 771 cm^{-1}. The most interesting band is located at 660 cm^{-1} corresponding to bending band in CO_2 molecule. Consequently, the CO_2 gas generation can be monitored throughout the cycling of the cell in *operando* conditions. The CO_2 band is detected positive at the open circuit voltage (OCV) (figure S2), which confirms that the CO_2 generation is mainly due to the catalytic properties of the Ti^{4+} (chemical reactivity of LTO electrode) and not related to electrochemical phenomenon[10]. The fluorination fades readily the CO_2 generation in OCV, thus the surface fluorination of the LTO leads to protect the electrolyte from the catalytic properties of the Ti^{4+}. From the observation of the spectra recorded during the first cycle (figure 4), it appears that CO_2 are continuously generated in charge and discharge, even with fluorinated electrodes. But in the case of the *HighF* electrodes, the band intensities due to the gas generation is 5 times lower in the cell than in the case of *NoF* electrodes during the first charge/discharge cycle. Same observations are made for the second and the tenth cycle gives 5 times and 3 times lower CO_2 generation for *HighF* electrodes during the second and the tenth cycle respectively, in agreement with the first cycle. Therefore, the surface fluorination of LTO is efficient to prevent the CO_2 gas generation during the cycling.

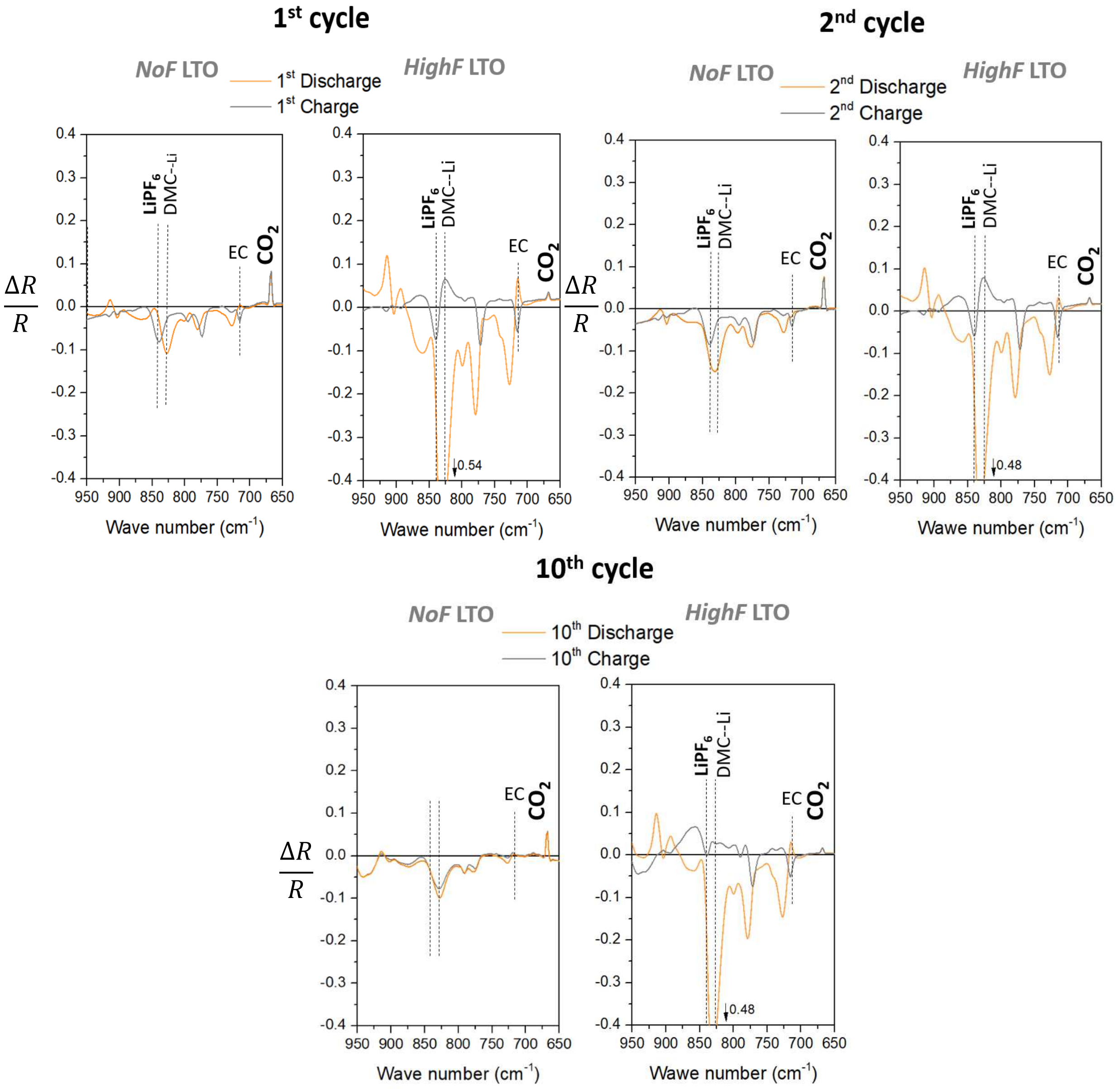

Figure 4 : ATR-FTIR spectra recorded between 950 and 650 cm^{-1} for electrolytes LP30 without additives in the neighborhood of NoF and HighF electrodes for the 1st, 2nd and 10th charge (in grey)/discharge (in orange) cycle. The spectra are displayed in relative intensities: positives bands for formed species and negatives bands for consumed species.

GC-MS analysis

Electrolytes are collected from cycled cells at different state of charge (SOC) to compare gases dissolved into the electrolyte with GC-MS. Full length chromatograms are shown is supporting (figure S3), the DMC and EC solvent peak are clearly identified, in addition to some electrolyte by-products. For all samples, the area of the DMC solvent peaks is used as a reference and CO_2/DMC area ratios are calculated to follow the evolution of CO_2 quantity (figure 5 a). Electrolytes collected after OCV from *HighF* compound containing cells exhibit

3 times less CO_2 dissolved into the electrolyte than half-cells with *NoF* electrodes. The same trend is observed after completing the first discharge with 4 times less CO_2 (figure 5 b) and after the charge with 1.4 time less CO_2 dissolved in the electrolyte, which is consistent with the previous ATR-FTIR results.

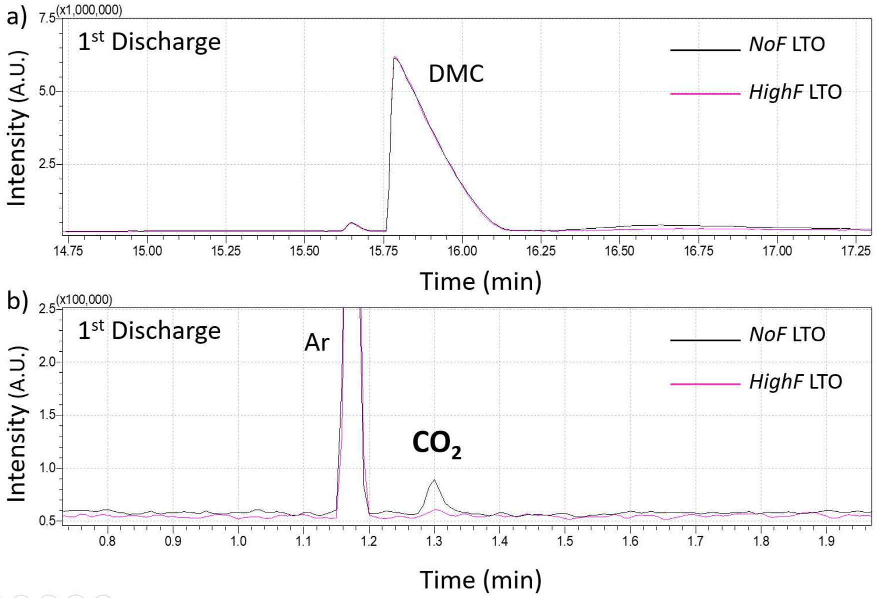

Figure 5: GC-MS chromatograms recorded for LP30 electrolytes collected after completing the first discharge in NoF and HighF half-cells.

1.2. SEI study of fluorinated LTO

The fluorination of the LTO surface is responsible of a significant reduction of the CO_2 gas production that could be related to a lower surface reactivity with the electrolyte. In order to investigate the surface reactivity of fluorinated electrodes and the SEI properties, XPS analysis are performed with an aluminum Kα X-Ray source on cycled electrodes stopped at different SOC for the first and the tenth cycles (Figures S4, S5, S6 and S7). XPS has already proved to be a powerful tool to investigate cycled electrodes and SEI nature formed on electrodes surfaces[40,41]. The cells prepared for XPS analysis are cycled at a slow C-rate (0.2 C) to form a well-established SEI, without electrode kinetic restrictions. Also the cells are cycled in half cell, namely the LTO is cycled as a positive electrode, thus the first step consists of a discharge from the OCV potential to 1.0 V *vs.* Li^+/Li and the first cycle is ended by a charge until 2.5 V *vs.* Li^+/Li. The quantitative results are displayed in Tables S1, S2 and S3.

The F1s spectrum (figure 6) of the *NoF* starting electrode, exhibits one component located at 687.3 eV attributed to CF_2 environments from the PVDF binder. The fluorination of the LTO active material leads to form Li-F species on surface, identified by the additional component at 684.9 eV observed for both *LowF* and *HighF*. Indeed, the reaction between the fluorine and the LTO lithium is strongly thermodynamically promoted. Also Ti 2p spectra show the formation of a solid solution $Li_{4-x}Ti_5O_{12-x}F_x$ already identified in (figure S4). The fluorination of the LTO is accounting for 4.4 at% and 8.0 at% of the electrode surface for *LowF* and *HighF* respectively with the Al Kα source (Table S1). $F_{fluorination}$/Ti ratios are calculated up to 0.54 and 0.98 for *LowF* and *HighF* respectively.

In addition to the aluminum XPS analysis, we carried out silver XPS analysis with an experimental setup allowing to use both monochromatised aluminum Kα and silver Lα X-ray sources integrated in the same equipment. Both analyses with the two X-Ray sources are performed on the exactly same point of the same electrode sample for reproducibility. The aluminum Kα source is able to probe around 10 nm in depth while the silver Lα is able to probe around 20 nm, without any etching. As the Relative Sensivity Factors (RSF) for Ag Lα X-ray source are still widely discussed in the literature, we based our XPS quantifications on RSF recently calculated by Shard *et al.*[42] The comparison of the quantifications from Al Kα and Ag Lα analysis give insights about the localization of the species in depth. The objective is to provide information about the nature of the surface fluorination at different depths.

The comparison with the spectra recorded with the silver source exhibits a deeper fluorination diffusion in the case of the *HighF* compound (Figure 6). The atomic percentage of Li-$F_{fluorination}$ drops, with the deeper analysis, 12.6 at% and 3.8 at% in the whole F 1s signal for *LowF* and *HighF* respectively, as well as Fluorination/Ti ratios (0.28 for *LowF* and 0.60 for *HighF*), proving that the fluorination is located on the extreme surface of the LTO particles. Note that a stronger fluorine diffusion within LTO material is observed with the *HighF* fluorination conditions.

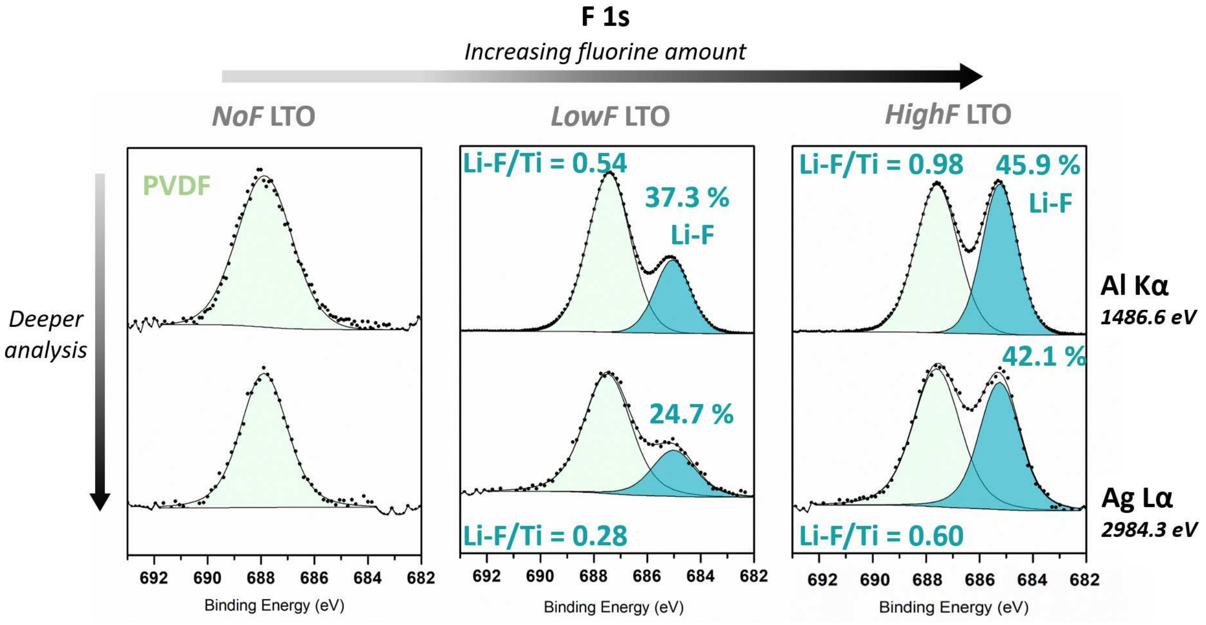

Figure 6 : F1s high resolution spectra recorded for NoF, LowF and HighF fresh electrodes recorded with two X-ray sources Al Kα and Ag Lα. Relative percentage of Li-F over the fluorine total amount are displayed.

XPS analysis are carried out on cycled electrode using the Al Kα X-Ray source (figure 8) in order to evaluate the efficiency of the fluorination coating (detailed quantification tables are provided in supporting information Tables S1, S2 and S3). The surface species are quantified and separated in two main contributions: the electrode species and the ones constituting the SEI layer. The quantification of the species belonging to the electrode is the addition of carbon black, PVDF (identified in C 1s and F 1s spectra) and LTO contributions (with related components in Ti 2p (figure S4), O 1s (figure S5) and Li 1s spectra (not shown here).

After Open Circuit Voltage (OCV)

After two hours of OCV, electrodes (fluorinated or not) exhibit surface reactivity toward the electrolyte by direct contact, without electrochemical process involved. The *NoF* surface is covered by carbonates specie (43.8 at%) and Li-F$_{\text{Surface species}}$ (11.5 at%) (Figure 8). The electrode is still detected after the deposition of surface species. Note that the carbon contamination (Table S1) remains similar which allows the comparison of quantitative analysis between compounds. The fluorinated electrodes are less reactive with the electrolyte. Indeed, the fluorinated electrodes contributions (46.6 at% for *LowF*, 55.9 at% for *HighF*) are higher than the *NoF* one (44.1 at%), testifying less surface covering species. Lower content of carbonate is observed on *HighF* electrodes (37.1 at%) in comparison with *NoF* electrodes (43.8 at%) and lower content of Li-F$_{\text{Surface species}}$ are observed on both fluorinated electrodes, from 11.5 at% for *NoF* to 7.2 at% and 6.6 at% for *LowF* and *HighF* respectively *(Figure 8)*. Thus, the fluorination limits the reactivity of electrode with the electrolyte and thus degradation products deposition.

Complementary, electrodes are analyzed with the Ag X-Ray source (figure S8). The carbonate species are located on the extreme surface as the contribution of the electrode (Carbon black related components) to the C1s signal is increasing, on both *NoF* and *HighF* samples, with the deeper analysis. Contrariwise, the Li- $F_{\text{Surface species}}$ forms a relatively thick layer as its proportion does not change. This indicates that the Li-$F_{\text{surface species}}$ are located close to the electrode while carbonate species are more located at the extreme surface. For the *HighF* electrode, the Li-$F_{\text{Surface species}}$ proportion originated from the contact with the electrolyte is estimated knowing that the Fluorination/Ti ratio is equal to 0.98 (Figure 6) and assuming it remains unchanged after the OCV. The analysis with the silver source reveals that the Li-$F_{\text{Surface species}}$ proportion increases with the depth of the analysis but remains lower than the proportions observed on the *NoF* electrode. In every cases, the raw electrode is more detected with the Ag X-Ray source. From the observation of the XPS analysis after OCV, we can conclude that the fluorination protects the electrode from the reactivity with the electrolyte.

First discharge

The first discharge leads to a deposition on the electrode surfaces as the formation process of the SEI is initiated by the decreasing electrochemical potential. The SEI thickness freshly formed cannot be measured directly by XPS, but we estimate thickness below 10 nm since the active material is still detected. Regarding the C1s spectra (Figure S6), the discharged *NoF* electrode exhibits a weak carbon black component located at 283.6 eV and accounting for 8.1 % of the total carbon signal (Table S2). The -CH_2-CF_2-environments, observed at 286.3 eV and 290.7 eV with the same area allow the PVDF identification and account for the electrode quantification. The O 1s spectra (figure S5) exhibits a peak located at 529.8 eV attributed to the O^{2-} from the LTO material. Two additional components are detected at 531.8 eV and 533.5 eV corresponding to C=O and C-O bonds respectively originated from electrolyte degradation products. After the first discharge, F 1s *NoF* spectrum (Figure S7) exhibits two components: one located at 685.2 eV and 688.0 eV corresponding to Li-F environments coming from salt degradation and from the -CF_2-CH_2- groups of the PVDF binder. As foreseen with the OCV observations, the fluorinated electrodes surfaces are less reactive since the SEI proportions detected on the surface are lower. The *LowF* and *HighF* electrodes exhibit 44.6 at% and 47.1 at% of electrode proportions against 42.3 at% for the bare LTO electrode (figure 8). The fluorination passivates the electrodes surfaces from carbonate and salt degradation products since the fluorinated electrodes are less covered than the *NoF* electrode one after the first discharge completion. The carbonate quantification is decreasing from 47.6 at% for *NoF* to 44.7 at% for *HighF* and the Li-F_{SEI} is also decreasing from 9.7 at% for *NoF* to 7.2 at% for *HighF*.

Once again, Ag Lα X-ray source is used to give further insights about the species localization within the SEI thickness. The figure 7 presents the F 1s and C 1s XPS spectra for *NoF* and *HighF* for electrodes collected after the first discharge. As mentioned for OCV, silver XPS analysis reveal that the carbonated species are mainly located on the extreme surface as the electrode signal is stronger with the depth of the analysis, contraries to the Li-F_{SEI} species. Indeed, after the first discharge, the Li-F_{SEI} proportion in the SEI is nearly homogeneous for at least the 20 first nanometers. This observation is consistent with 3D depth profiles performed in the literature on cycled LTO electrodes by ToF-SIMS.[43] From all the observations made at the end of the first discharge, the Li-F formation on LTO surface, by the mean of the XeF_2 fluorination, appears to effectively protect the surface from strong side reactions and prevent the formation of a too thick SEI layer.

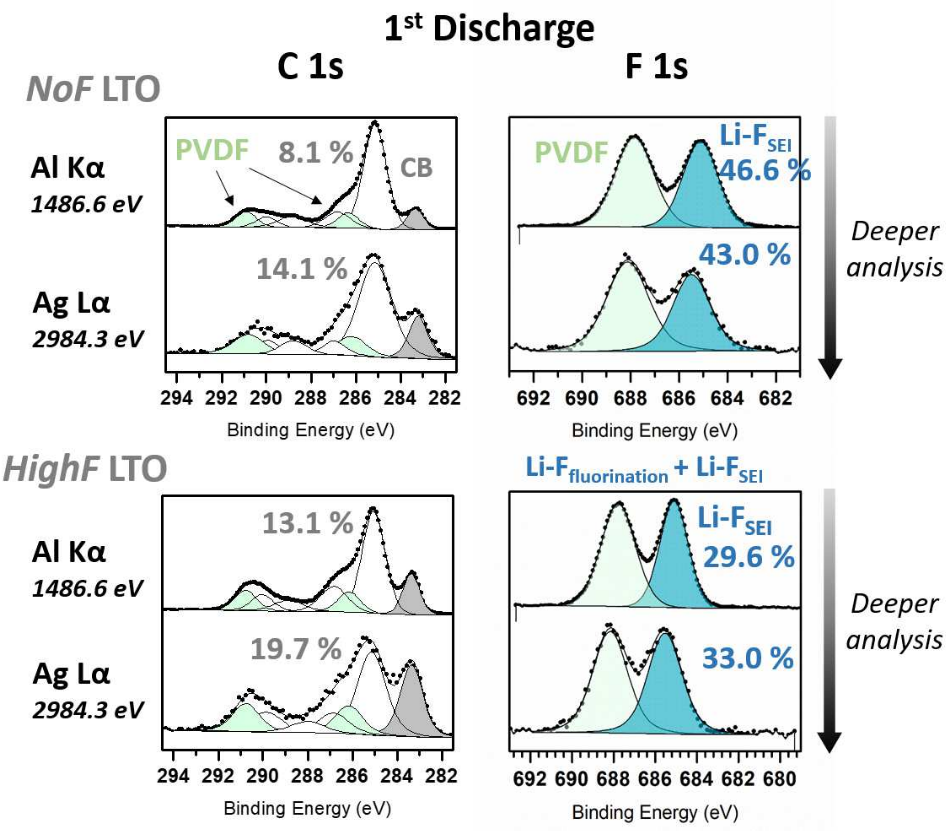

Figure 7 : XPS Al Kα and Ag Lα C 1s and F 1s spectra recorded after completion of the first discharge for NoF and HighF electrodes. Carbon black (CB) and Li-F environments originated from the SEI formation relative percentages are given.

First charge

After the first charge, the high potential reached (2.5 V *vs.* Li^+/Li) causes a partial dissolution of the SEI. The SEI of the *NoF* electrode undergoes a strong dissolution in charge, the SEI quantification drops by nearly 10 at% in comparison with the first discharge (Figure 8), to reach a thickness even lower than the layer formed after OCV. The Li-F_{SEI} specie, dissolved in charge, is more impacted than the carbonate species. The fluorination limits this dissolution, indeed the *LowF* SEI is barely dissolved (SEI quantification decrease by 0.2 at% (Figure 8)) and the *HighF* SEI quantification reach very similar quantification values than the OCV (surface species accounts for 44.1 at% after OCV and the SEI for 44.0 at% after the first charge).

The analysis of the first cycle (OCV + first discharge + first charge) shows the faded surface reactivity of fluorinated electrodes. The deposition of surface species, carbonate or salt degradation products, are reduced by the fluorination for the first cycle. The SEI formed on fluorinated electrodes appears thinner and more stabilized.

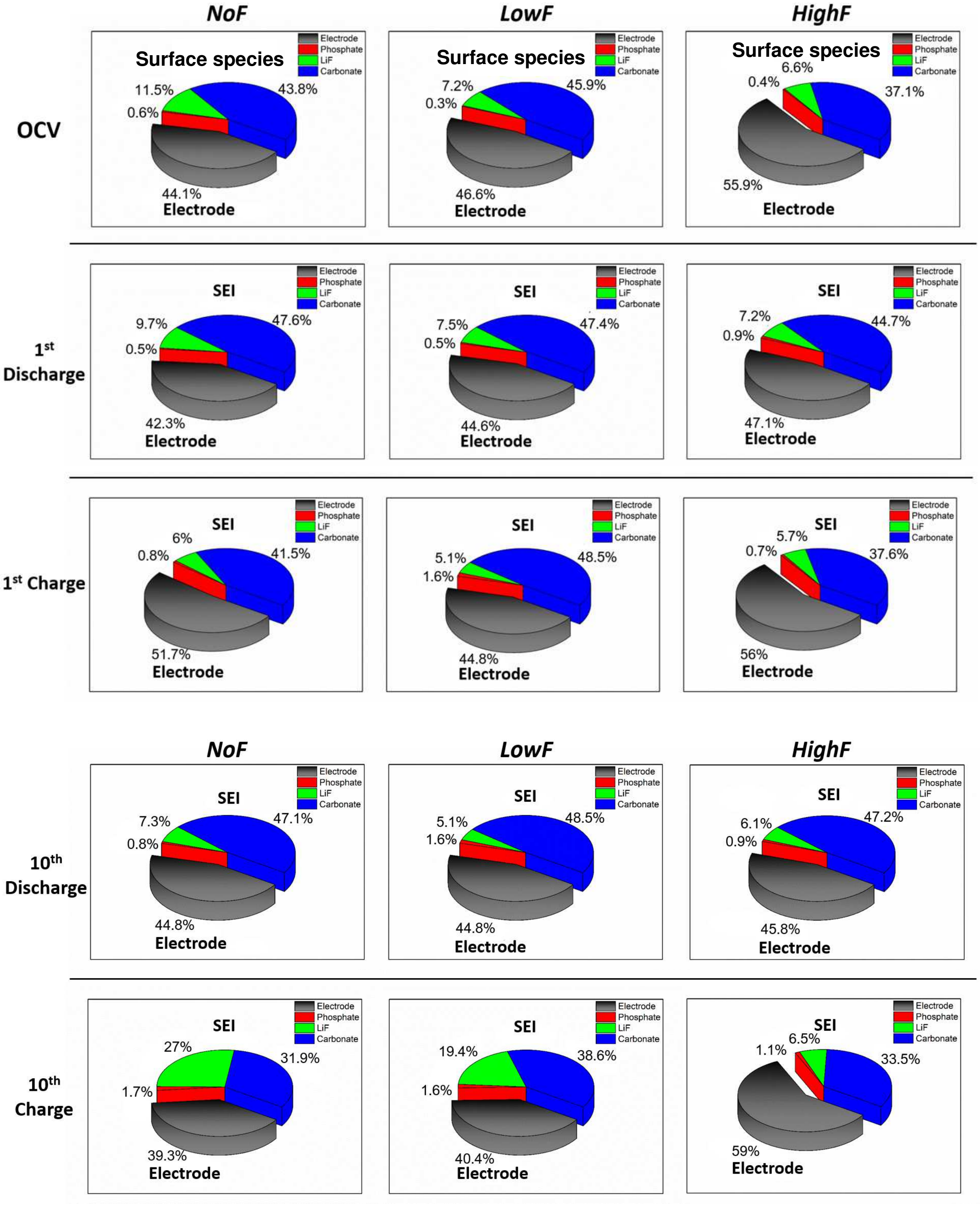

Figure 8 : XPS quantification of Electrodes species (LTO material, carbon black and PVDF) and SEI species (carbonates, LiF and phosphate) after OCV, 1st Discharge, 1st Charge, 10th Discharge and 10th Charge.

Tenth cycle

The 10th discharge drives to the formation of the SEI for all the electrode surfaces. After ten cycles, the quantification values are quite homogenized between the *NoF* electrode and the fluorinated ones (figure 8 and table S3). Since the SEI formation processes occur mainly during the first cycles, after ten cycles the SEI are now well established and the surfaces converge on similar composition and thickness, but the specific capacities remain higher for *HighF* electrodes. The covering values after both the 10th discharge and charge for NoF electrodes show a thicker SEI than the ones observed for the first cycle. The fluorination lead stabilized the SEI formation after the few first cycles. Indeed, in the case of the *HighF* electrodes, the covering values after the tenth cycle are very similar to the first cycle. Moreover, after the 10th charge, the salt degradation products increase in the SEI quantification but Li-F_{SEI} specie is still less detected on fluorinated electrodes.

Conclusion

From the observations and the discussions previously given, the influence of the surface fluorination of $Li_4Ti_5O_{12}$ material by the mean of XeF_2 decomposition appears clearly to be beneficial regarding several aspects.

A threshold amount of fluorine need to be reached in order to observe modifications of the LTO electrochemical behavior, since the *LowF* LTO compound provides little significant improvements in terms of specific capacities. The fluorine-rich compound, *HighF* LTO, exhibits improved specific capacities of 180 mAh.g^{-1}, around 12% more than bare LTO electrodes for 100 hundred cycles with a relatively good stability. The extra specific capacity can be related to fluorinated surface species. The *HighF* LTO exhibit improved rate capability from 0.5 to 15 C-rate and the specific capacities recovered after the C-rate remain higher than the *NoF* LTO. The *LowF* LTO undergoes stronger capacity fading at high C-rate related to higher polarization.

Fluorinated electrodes clearly influence solvation shells within the electrolyte in the neighborhood of the electrode. The reversible solvation/desolvation process of Li in electrolyte solvent is promoted by modifying the intermolecular energy of solvation shells. ATR-FTIR results demonstrated that the CO_2 gas generation is drastically reduced by the fluorination from the OCV to the tenth cycle, during both charge and discharge. These results are confirmed by relative dissolved CO_2 quantities detected with GC-MS measurements.

From the pristine electrode comparison, Li-F is the main species identified from the surface fluorination process of LTO. A solid solution $Li_{4-x}Ti_5O_{12-x}F_x$ is also observed from the Ti 2p spectra. The fluorine is quantified on surface up to 4.4 at% and 8.0 at% for *LowF* and *HighF* electrodes respectively. The *HighF* fluorination condition leads to deeper fluorine diffusion in the $Li_4Ti_5O_{12}$ material. The analysis of the first cycle shows that a thick layer of LiF originated from the salt degradation, and it shows that fluorination prevents its formation on electrode surface by halving the LiF proportion after the 1st discharge. The carbonate species appear to be localized on the extreme surface. A strong covering by carbonate species is observed straight away the OCV and a still stronger covering is observed after the first discharge. The *HighF* fluorination reduces the carbonate covering after OCV and the 1st discharge. The fluorination, in both *LowF* and *HighF* conditions, conducts to fade the surface reactivity of the electrode toward the electrolyte. The SEI quantification decreases on fluorinated electrodes, and the SEI stability against dissolution is improved. The quantification values seem to homogenize after ten cycles.

Outlooks of this study could be the investigation of the fluorination influence of the previously discussed aspects at high temperature. Switch to molecular fluorination using F_2 should be consider for up-scale synthesis.

Acknowledgements: The authors thank the French National Research Agency for the financial support (STORE-EX Labex Project ANR-10-LABX-76-01).

References

1. K. M. Colbow, J. R. Dahn, and R. R. Haering, *J. Power Sources*, **26**, 397–402 (1989).

2. T. Ohzuku, A. Ueda, and N. Yamamoto, *J. Electrochem. Soc.*, **142**, 1431–1435 (1995).

3. K. Zaghib et al., *J. Power Sources*, **196**, 3949–3954 (2011).

4. M. Winter et al., *Monatshefte Für Chem. Chem. Mon.*, **132**, 473–486 (2001).

5. J. Christensen, V. Srinivasan, and J. Newman, *J. Electrochem. Soc.*, **153**, A560–A565 (2006).

6. M.-S. Song et al., *J. Mater. Chem. A*, **2**, 631–636 (2013).

7. F. Shi et al., *J. Am. Chem. Soc.*, **137**, 3181–3184 (2015).

8. G.-N. Zhu et al., *Adv. Funct. Mater.*, **23**, 640–647 (2013).

9. L. Zhao, Y.-S. Hu, H. Li, Z. Wang, and L. Chen, *Adv. Mater.*, **23**, 1385–1388 (2011).

10. Y.-B. He et al., *Sci. Rep.*, **2**, 913 (2012).

11. S. S. Zhang, *J. Power Sources*, **162**, 1379–1394 (2006).

12. P. K. Alaboina et al., *ACS Appl. Mater. Interfaces*, **8**, 12127–12133 (2016).

13. J. P. Olivier and M. Winter, *J. Power Sources*, **97–98**, 151–155 (2001).

14. R. Bernhard, M. Metzger, and H. A. Gasteiger, *J. Electrochem. Soc.*, **162**, A1984–A1989 (2015).

15. S. Kim et al., *RSC Adv.*, **8**, 32558–32564 (2018).

16. X. Huang, R. Ren, N. K. Singh, M. Hardi, and J. Chen, *ChemistrySelect*, **3**, 10792–10798 (2018).

17. C. P. Han et al., *Electrochimica Acta*, **157**, 266–273 (2015).

18. W. Li et al., *Electrochimica Acta*, **139**, 104–110 (2014).

19. M. R. Jo, G.-H. Lee, and Y.-M. Kang, *ACS Appl. Mater. Interfaces*, **7**, 27934–27939 (2015).

20. Y. Wang et al., *ACS Appl. Mater. Interfaces*, **8**, 26008–26012 (2016).

21. B. Fleutot et al., *Appl. Surf. Sci.*, **400**, 139–147 (2017).

22. T. Nakajima, M. Koh, R. N. Singh, and M. Shimada, *Electrochimica Acta*, **44**, 2879–2888 (1999).

23. T. Nakajima, A. Ueno, T. Achiha, Y. Ohzawa, and M. Endo, *J. Fluor. Chem.*, **130**, 810–815 (2009).

24. Y. Zhang et al., *ACS Appl. Mater. Interfaces*, **9**, 17145–17154 (2017).

25. Y. Charles-Blin et al., *ACS Appl. Energy Mater.* (2019) https://doi.org/10.1021/acsaem.9b01191.

26. J. G. Malm, H. Selig, J. Jortner, and S. A. Rice, *Chem. Rev.*, **65**, 199–236 (1965).

27. D. A. Shirley, *Phys. Rev. B*, **5**, 4709–4714 (1972).

28. G. Gachot et al., *Anal. Methods*, **6**, 6120–6124 (2014).

29. Z. Wang et al., *J. Electrochem. Soc.*, **143**, 1510–1514 (1996).

30. Z. Wang, X. Huang, and L. Chen, *J. Electrochem. Soc.*, **150**, A199–A208 (2003).

31. Y. Ikezawa and H. Nishi, *Electrochimica Acta*, **53**, 3663–3669 (2008).

32. J.-T. Li, S.-R. Chen, X.-Y. Fan, L. Huang, and S.-G. Sun, *Langmuir*, **23**, 13174–13180 (2007).

33. L. Doucey, M. Revault, A. Lautié, A. Chaussé, and R. Messina, *Electrochimica Acta*, **44**, 2371–2377 (1999).

34. R. Aroca, M. Nazri, G. A. Nazri, A. J. Camargo, and M. Trsic, *J. Solut. Chem.*, **29**, 1047–1060 (2000).

35. J.-T. Li et al., *J. Electroanal. Chem.*, **649**, 171–176 (2010).

36. J.-T. Li, Z.-Y. Zhou, I. Broadwell, and S.-G. Sun, *Acc. Chem. Res.*, **45**, 485–494 (2012).

37. C. Marino et al., *J. Phys. Chem. C*, **121**, 26598–26606 (2017).

38. O. Borodin et al., *Phys. Chem. Chem. Phys.*, **18**, 164–175 (2015).

39. L. Madec et al., *Phys. Chem. Chem. Phys.*, **17**, 27062–27076 (2015).

40. J.-B. Gieu, C. Courrèges, L. El Ouatani, C. Tessier, and H. Martinez, *J. Power Sources*, **318**, 291–301 (2016).

41. J.-B. Gieu, C. Courrèges, L. E. Ouatani, C. Tessier, and H. Martinez, *J. Electrochem. Soc.*, **164**, A1314–A1320 (2017).

42. A. G. Shard et al., *Surf. Interface Anal.*, **51**, 763–773 (2019).

43. J.-B. Gieu et al., *J. Mater. Chem. A*, **5**, 15315–15325 (2017).

LTO NoF

LTO-F

Atomic layer fluorination by the mean of XeF$_2$

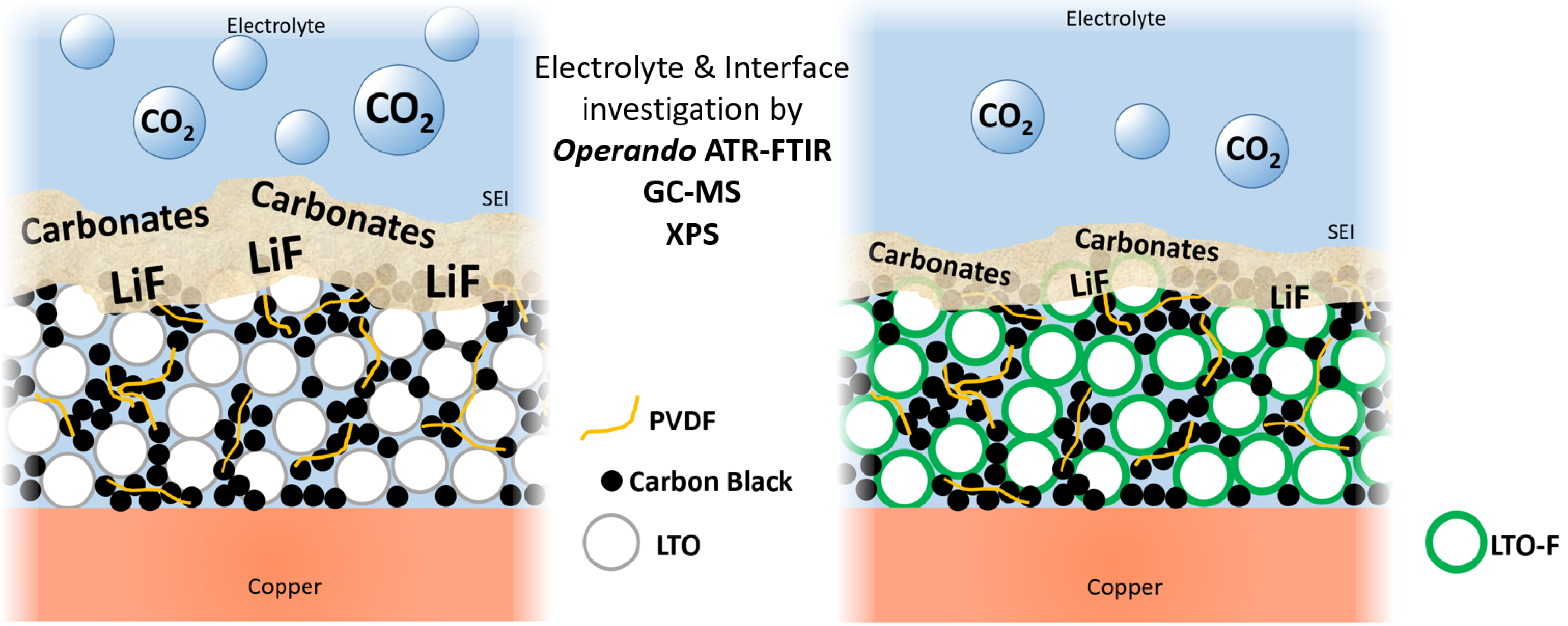

Electrolyte & Interface investigation by

Operando **ATR-FTIR**

GC-MS

XPS